New Journal of Physics
The open access journal at the forefront of physics

Deutsche Physikalische Gesellschaft DPG IOP Institute of Physics

PAPER • OPEN ACCESS

Creutz ladder in a resonantly shaken 1D optical lattice

To cite this article: Jin Hyoun Kang *et al* 2020 *New J. Phys.* **22** 013023

New Journal of Physics
The open access journal at the forefront of physics

Deutsche Physikalische Gesellschaft DPG
IOP Institute of Physics

Published in partnership with: Deutsche Physikalische Gesellschaft and the Institute of Physics

OPEN ACCESS

RECEIVED
8 July 2019

REVISED
2 December 2019

ACCEPTED FOR PUBLICATION
13 December 2019

PUBLISHED
20 January 2020

PAPER

Creutz ladder in a resonantly shaken 1D optical lattice

Jin Hyoun Kang[1,2], **Jeong Ho Han**[1,2] **and Y Shin**[1,2]

[1] Department of Physics and Astronomy, and Institute of Applied Physics, Seoul National University, Seoul 08826, Republic of Korea
[2] Center for Correlated Electron Systems, Institute for Basic Science, Seoul 08826, Republic of Korea

E-mail: yishin@snu.ac.kr

Keywords: Creutz ladder model, periodically driven optical lattice, ultracold fermions in optical lattices, topological ladder

Abstract

We report the experimental realization of a Creutz ladder for ultracold fermionic atoms in a resonantly driven 1D optical lattice. The two-leg ladder consists of the two lowest orbital states of the optical lattice and the cross inter-leg links are generated via two-photon resonant coupling between the orbitals by periodic lattice shaking. The characteristic pseudo-spin winding structure in the energy bands of the ladder system is demonstrated using momentum-resolved Ramsey-type interferometric measurements. We discuss a two-tone driving method to extend the inter-leg link control and propose a topological charge pumping scheme for the Creutz ladder system.

1. Introduction

Topological phases such as quantum Hall states and topological insulators represent intriguing physics beyond the conventional Landau paradigm of phase transition [1, 2]. Motivated further by their novel transport properties, the study of topological phases constitutes one of the frontiers in modern condensed matter physics. Ultracold atoms in optical lattices, featuring tunneling amplitude engineering and tunable interaction strength, provide a unique platform for realizing and exploring such exotic topological states [3, 4]. Along with the steady development of experimental techniques, many topological model systems have been recently realized, which include the Harper–Hofstadter Hamiltonian in 2D rectangular lattices [5, 6], the Haldane model in a 2D hexagonal lattice [7], and various Hall and topological ladder systems based on additional synthetic dimensions such as internal atomic states [8–13] and lattice orbital states [14].

Periodic lattice shaking is one of the successful tools for exploring exotic phases in optical lattices. Under periodic modulations of the lattice potential, the system parameters such as tunneling magnitude [15, 16] and phase [17] can be coherently manipulated, giving rise to a hopping configuration that is difficult to realize with static schemes. An outstanding example is the Haldane model realized by circularly shaking a 2D hexagonal optical lattice potential to achieve complex next-nearest-neighbor hopping [7, 18]. From the perspective of Floquet band engineering, the lattice shaking method has been extensively discussed even in the resonant regime where the driving frequency is high enough to match the energy gap between two bands [19]. Such strong orbital hybridization may enable access to a broader range of effective Hamiltonians [20, 21]. In particular, it was anticipated that multi-photon inter-orbital resonant coupling could yield a special route to engineer topological states [22, 23]. Thus, it is highly desirable to examine the multifarious scope of Floquet band engineering for the study of topological phases.

In this paper, we experimentally investigate the effects of two-photon inter-orbital resonant coupling in a periodically driven 1D optical lattice, and demonstrate the realization of a generalized Creutz ladder for ultracold fermionic atoms in the shaken lattice system. The Creutz ladder is a cross-linked two-leg ladder system under a magnetic field, which has been discussed as a minimal model for 1D topological insulators [24–26]. Recently, it was extended to an interacting case, referred to as the Creutz–Hubbard model, for the study of correlated topological phases [27–31]. In our experiment, the two-leg ladder is formed by the two lowest orbital states in optical lattice, and the cross inter-leg links are generated via the two-photon resonant coupling between the orbitals by lattice shaking. Using momentum-resolved Ramsey-type interferometric measurements, we demonstrate the characteristic pseudo-spin winding structure in the energy bands of the Creutz ladder. We also

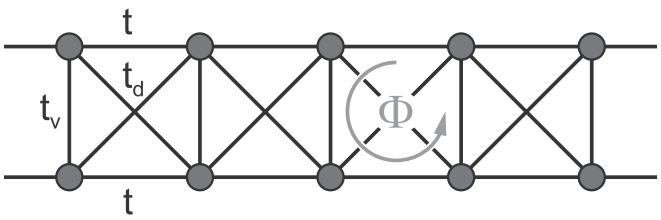

Figure 1. Creutz ladder model. A two-leg ladder system under a magnefic field. t denotes the intra-leg hopping amplitude and Φ is the gauge flux per plaquette. t_v and t_d indicate the inter-leg hopping amplitudes in the ladder along the vertical rungs and the diagonal links, respectively.

discuss the extension of the inter-leg link control with two-frequency driving, where the direct links are additionally controlled by the one-photon resonant coupling between the orbitals. Finally, based on the extented inter-leg link control, we propose an experimental scheme for topological charge pumping in the generalized Creutz ladder system.

2. Creutz ladder model

The Creutz model describes a spinless fermion system in a two-leg ladder under a magnetic field [24]. The two-leg ladder system is sketched in figure 1, where t denotes the hopping amplitude along the legs, t_v along the rungs of the ladder, t_d along the diagonal links, and Φ is the gauge flux penetrating each ladder plaquette. The system's Hamiltonian is given by

$$H_{\mathrm{CL}} = \sum_j [\{\Psi_j^\dagger (t e^{-\mathrm{i}(\Phi/2)\sigma_z} + t_d \sigma_x)\Psi_{j+1} + \mathrm{h.c.}\} + \Psi_j^\dagger (t_v \sigma_x)\Psi_j], \tag{1}$$

where $\Psi_j = (c_{j,1}, c_{j,2})^{\mathrm{T}}$ with $c_{j,l}$ being the annihilation operator of the fermion at site j and leg $l \in \{1, 2\}$, and $\boldsymbol{\sigma} = \{\sigma_x, \sigma_y, \sigma_z\}$ are the Pauli matrices. The corresponding Bloch Hamiltonian is expressed as

$$\begin{aligned} H_{\mathrm{CL},q} &= 2t\cos(\Phi/2)\cos(q)\mathbb{I} + [t_v + 2t_d\cos(q)]\sigma_x + 2t\sin(\Phi/2)\sin(q)\sigma_z \\ &= 2t\cos(\Phi/2)\cos(q)\mathbb{I} + \boldsymbol{h}_{\mathrm{CL}}(q)\cdot\boldsymbol{\sigma}, \end{aligned} \tag{2}$$

where q is the quasimomentum, $\mathbb{I}$ is the identity matrix, and $\boldsymbol{h}_{\mathrm{CL}}(q) = \{t_v + 2t_d\cos(q),\ 0,\ 2t\sin(\Phi/2)\sin(q)\}$. Because the vector $\boldsymbol{h}_{\mathrm{CL}}$ is confined in the xz plane, its winding around the origin for the whole Brillouin zone (BZ), $-\pi < q \leqslant \pi$, characterizes the topology of the ladder system. A topologically non-trivial state occurs when $|t_v/t_d| < 2$, where $\boldsymbol{h}_{\mathrm{CL}}(q)$ fully encircles the origin, giving a non-zero integer winding number representing the topological character of the system. The band dispersion of the system is given by $E_\pm(q) = 2t\cos(\Phi/2)\cos(q) \pm |\boldsymbol{h}_{\mathrm{CL}}(q)|$. It is remarkable that with $\Phi = \pi$, $t_v = 0$ and $t_d = t$, the ladder system has $E_\pm(q) = \pm 2|t|$, constituting a 1D topological system with two flat bands.

The original Creutz model was proposed for a special case of $\Phi = \pm\pi$, where the ladder system holds chiral symmetry for $\sigma_y H_{\mathrm{CL},q}\sigma_y = -H_{\mathrm{CL},q}$ [24], and it is equivalent to the Su–Schrieffer–Heeger model, which belongs to the BDI class of the Altland–Zirnbauer classification [30, 32]. In an extended case of $\Phi \neq \pm\pi$, the chiral symmetry is broken, but since $\boldsymbol{h}_{\mathrm{CL}}$ remains in the xz plane, the topological character of the system is still unambiguously represented by the winding number of $\boldsymbol{h}_{\mathrm{CL}}$. It was discussed that the topological phase of the extended Creutz model is protected by a hidden inversion symmetry [33, 34].

3. Atom in a resonantly shaken optical lattice

We consider an atom in a 1D optical lattice potential $V(x) = \frac{V_L}{2}\cos[\frac{2\pi}{a}(x - x_0)]$, where the position x_0 of the lattice potential is periodically driven as $x_0(t) = -\mathrm{d}\cos(\omega t + \varphi)$ [figure 2(a)]. Here, V_L is the lattice depth and a is the lattice spacing. In the comoving reference frame with the vibrating optical lattice, the Hamiltonian of the system is given by $H = H_{\mathrm{stat}} + \delta H$ with

$$\begin{aligned} H_{\mathrm{stat}} &= \frac{p_x^2}{2m} + \frac{V_L}{2}\cos\left(\frac{2\pi}{a}x\right), \\ \delta H &= -\mathrm{d}\omega\sin(\omega t + \varphi)p_x, \end{aligned} \tag{3}$$

where H_{stat} is the Hamiltonian of the stationary optical lattice system with p_x being the atom's momentum and m being the atomic mass, and δH represents the perturbation from the inertial force induced by the lattice shaking, which can make mixing between the energy bands of the stationary lattice system. In this work, we are interested

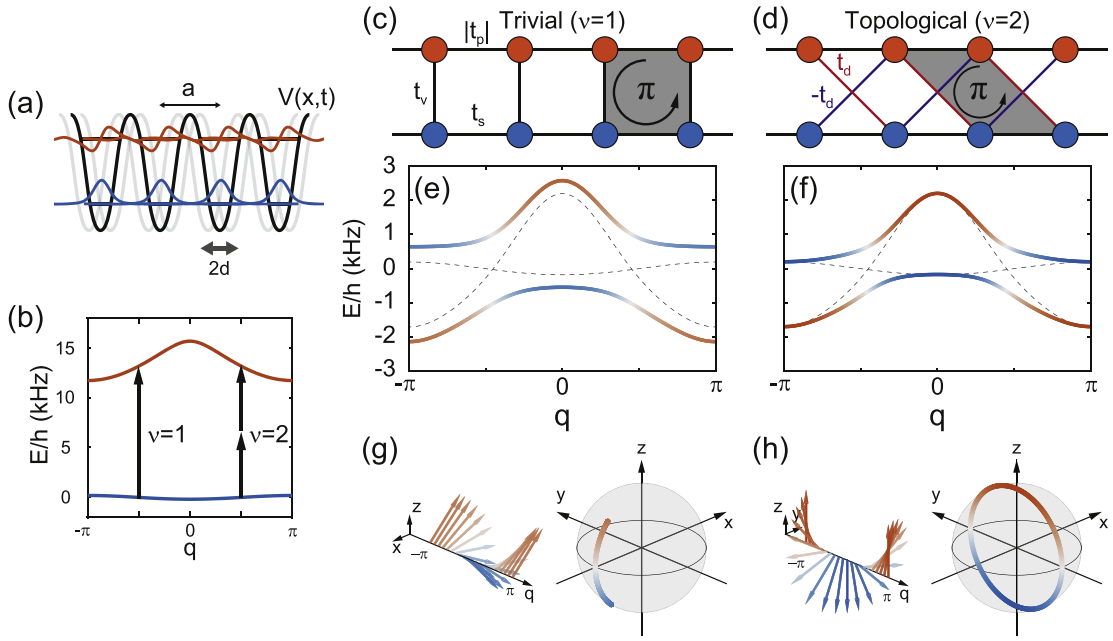

Figure 2. Creutz ladder in a resonantly shaken optical lattice. (a) Schematic of the periodically driven 1D lattice system. The position of the lattice potential is sinusoidally modulated with frequency ω and amplitude d. The lattice spacing is denoted by a. (b) The s and p orbitals can be resonantly coupled via one-photon ($\nu = 1$) or two-photon ($\nu = 2$) processes. Two-leg ladder diagrams for the systems with (c) the $\nu = 1$ and (d) $\nu = 2$ resonant couplings. Band structures of the ladder systems for our experimental conditions with (e) $\{\omega/2\pi, d/a\} = \{13.4\ \text{kHz}, 0.05\}$ and (f) $\{6.7\ \text{kHz}, 0.2\}$, giving $t_v/h = 1.0$ kHz ($\nu = 1$) and $t_d/h = 0.4$ kHz ($\nu = 2$), respectively. The blue and red colors indicate the orbital composition of the energy band, corresponding to s and p, respectively. The dashed lines show the bare dispersion curves of the s and p bands for $\{t_s, t_p\}/h = \{0.1, -1.0\}$ kHz. (g), (h) Corresponding pseudo-spin distributions of the ground bands and their trajectories on the Bloch sphere.

in the situation where the lattice shaking frequency ω is close to the resonance frequency for the coupling between the two lowest, s and p bands of the lattice potential (figure 2(b)). From a synthetic dimension perspective [35], the 1D shaken lattice system can be regarded as a two-leg ladder system constituted by the s and p orbitals, where the inter-orbital coupling by lattice shaking is depicted as the inter-leg links between the two legs.

In a two-band tight-binding approximation, the Hamiltonian of the driven lattice system is expressed as

$$H = \sum_j \Psi_j^\dagger K(t) \Psi_j - \sum_j [\Psi_j^\dagger J(t) \Psi_{j+1} + \text{h.c.}], \tag{4}$$

where $\Psi_j = (c_{j,p}, c_{j,s})^{\mathrm{T}}$, $c_{j,\alpha}$ is the annihilation operator for the atom in the Wannier state $|j, \alpha\rangle$ on lattice site j in orbital $\alpha \in \{s, p\}$. The matrices $K(t)$ and $J(t)$ are given by

$$K(t) = \begin{pmatrix} \epsilon_p & -\mathrm{i}h_0^{sp} \sin(\omega t + \varphi) \\ \mathrm{i}h_0^{sp} \sin(\omega t + \varphi) & \epsilon_s \end{pmatrix}$$
$$J(t) = \begin{pmatrix} t_p - \mathrm{i}h_1^{pp} \sin(\omega t + \varphi) & \mathrm{i}h_1^{sp} \sin(\omega t + \varphi) \\ -\mathrm{i}h_1^{sp} \sin(\omega t + \varphi) & t_s - \mathrm{i}h_1^{ss} \sin(\omega t + \varphi) \end{pmatrix}, \tag{5}$$

where $\epsilon_\alpha = \langle j, \alpha | H_{\text{stat}} | j, \alpha \rangle$ and $t_\alpha = -\langle j, \alpha | H_{\text{stat}} | j+1, \alpha \rangle$ are the on-site energy and nearest-neighbor hopping amplitude of the α orbital, respectively, and $h_\ell^{\alpha\beta} = \hbar\omega d \langle j, \alpha | (\partial/\partial x) | j + \ell, \beta \rangle$ is the transition element between the α and β orbitals separated by ℓ lattice sites [22].

When the shaking frequency ω is close to ω_{sp}^0/ν with integer ν, where $\omega_{sp}^0 = \epsilon_{sp}/\hbar$ and $\epsilon_{sp} = \epsilon_p - \epsilon_s$, a resonant inter-orbital coupling would be generated via ν-photon transition process. To explicate the properties of the inter-orbital couplings generated by the one-photon ($\nu = 1$) and two-photon ($\nu = 2$) resonant processes, we calculate the effective Hamiltonian $H_{\text{eff}}^{(\nu)}$ of the system in a rotating frame with frequency $\nu\omega$, using a high-frequency expansion method (appendix A) [36–38]. The effective Hamiltonian is obtained as $H_{\text{eff}}^{(\nu)} = H_0^{(\nu)} + H_C^{(\nu)}$ with

$$H_0^{(\nu)} = \sum_j \{\Psi_j^\dagger(\Delta_\nu \sigma_z)\Psi_j - [\Psi_j^\dagger(\bar{t}_r \mathbb{I} + t_r \sigma_z)\Psi_{j+1} + \text{h.c.}]\}$$
$$H_C^{(1)} = \sum_j \Psi_j^\dagger\left(\frac{h_0^{sp}}{2} R_{\hat{\boldsymbol{z}}}(\varphi)\sigma_x\right)\Psi_j$$
$$H_C^{(2)} = \sum_j \left[\Psi_j^\dagger\left(\frac{h_0^{sp} h_1}{2\hbar\omega} R_{\hat{\boldsymbol{z}}}(2\varphi) \mathrm{i}\sigma_y\right)\Psi_{j+1} + \text{h.c.}\right], \tag{6}$$

where $\Delta_\nu = \hbar\,(\omega_{sp}^0 - \nu\omega)/2$, $\bar{t}_r = \frac{t_p + t_s}{2}$, $t_r = \frac{t_p - t_s}{2}$, $R_{\hat{\boldsymbol{n}}}(\eta) = \exp(-\mathrm{i}\eta\hat{\boldsymbol{n}}\cdot\boldsymbol{\sigma})$ with $\hat{\boldsymbol{n}} = \boldsymbol{n}/|\boldsymbol{n}|$, and $h_1 = h_1^{pp} - h_1^{ss}$. $H_0^{(\nu)}$ represents an uncoupled two-leg ladder with energy imbalance Δ_ν and intra-leg hopping, and $H_C^{(\nu)}$ describes the dominant inter-leg coupling generated by the ν-photon resonant process.

The character of the inter-leg coupling given by $H_C^{(\nu)}$ is different for the two cases, $\nu = 1$ and $\nu = 2$. $H_C^{(1)}$ describes the on-site orbital-changing transitions, corresponding to the direct inter-leg links with amplitude $t_\nu = h_0^{sp}/2$ in the ladder system. On the other hand, $H_C^{(2)}$ describes the second-order processes consisting of on-site orbital changing and nearest-neighbor hopping along the leg direction, giving the diagonal inter-leg links with amplitude $t_d = h_0^{sp} h_1/2\hbar\omega$. The difference of $H_C^{(1)}$ and $H_C^{(2)}$ can be understood from parity conservation; since the lattice shaking is an odd-parity operation, the two-photon on-site transition is forbidden between the s and p orbitals, which have opposite parities [23]. In figures 2(c) and (d), we present the schematic diagrams of the resulting ladder systems for $\nu = 1$ and 2, respectively. Note that the sign of t_p is opposite to that of t_s, and under a proper transformation, the ladder systems can be viewed as having a π gauge flux piercing each ladder plaquette.

The Bloch Hamiltonian of the two-leg ladder system is expressed as $H_q^{(\nu)} = -2\bar{t}_r\cos(q)\mathbb{I} + \boldsymbol{h}_\nu(q)\cdot\boldsymbol{\sigma}$, where q is expressed in units of a^{-1} and the $\boldsymbol{h}_\nu(q)$ is given by

$$\boldsymbol{h}_1(q) = t_\nu\hat{\boldsymbol{\rho}}_1 + [\Delta_1 - 2t_r\cos(q)]\hat{\boldsymbol{z}}$$
$$\boldsymbol{h}_2(q) = 2t_d\sin(q)\hat{\boldsymbol{\rho}}_2 + [\Delta_2 - 2t_r\cos(q)]\hat{\boldsymbol{z}} \tag{7}$$

with $\hat{\boldsymbol{\rho}}_1 = \cos(\varphi)\hat{\boldsymbol{x}} + \sin(\varphi)\hat{\boldsymbol{y}}$ and $\hat{\boldsymbol{\rho}}_2 = -\sin(2\varphi)\hat{\boldsymbol{x}} + \cos(2\varphi)\hat{\boldsymbol{y}}$. Under a transformation of $\hat{\boldsymbol{\rho}}_\nu \to \hat{\boldsymbol{x}}$ and $q \to q - \frac{\pi}{2}$, the functional form of $H_q^{(\nu)}$ on q becomes same as that of $H_{\mathrm{CL},q}$ except the term of $\Delta_\nu\hat{\boldsymbol{z}}$ in $\boldsymbol{h}_\nu$. Regardless of having the additional term, $\boldsymbol{h}_\nu$ is confined in the plane defined by $\hat{\boldsymbol{\rho}}_\nu$ and $\hat{\boldsymbol{z}}$, and thus, its winding number determines the topological characteristic of the ladder system. From equation (7), it is obvious that $\boldsymbol{h}_1(q)$ cannot encircle the origin, whereas $\boldsymbol{h}_2(q)$ can give winding number of ± 1 when $|\Delta_2| < 2|t_r|$. This means that a topologically non-trivial phase would emerge in the shaken lattice system with two-photon resonant coupling ($\Delta_2 \approx 0$). The chiral symmetry is generally broken in $H_q^{(2)}$ due to $\bar{t}_r \neq 0$, and it was argued that the topologically non-trivial phase is protected by symmetry composed of time-reversal and mirror symmetries [12]. It is interesting to note that one of the topological bands becomes dispersionless when $|\Delta_2| = 2|\bar{t}_r|$ and $t_d^2 = |t_s t_p|$.

In figures 2(e) and (f), we display the band structures of the two-leg ladder system with one-photon resonant coupling ($\Delta_1 = 0$) and two-photon resonant coupling ($\Delta_2 = 0$), respectively. The pseudo-spin distributions of the ground bands over the BZ and their corresponding trajectories on the Bloch sphere are also shown in figures 2(g) and (h). In the $\nu = 2$ case, the pseudo-spin trajectory make a great circle on the Bloch sphere, which is the key topological feature of the constructed Creutz ladder system. In the following section, we present our experimental investigation, where the focus is to demonstrate the winding structure of $\boldsymbol{h}_2(q)$ in the resonantly shaken lattice system.

4. Experiment and result

4.1. Experimental setup

Our experiment starts with preparing a spin-balanced degenerate Fermi gas of ^{173}Yb atoms in the $F = 5/2$ hyperfine ground state, which has all the six spin components equally, in an optical dipole trap [39]. The total atom number is $\approx 1.5 \times 10^5$, and the temperature is $\approx 0.35 T_F$, where T_F is the Fermi temperature of the trapped sample. The atoms are adiabatically loaded in a 1D optical lattice potential, which is formed along the x-direction by interfering two laser beams with a wavelength of $\lambda_L = 532$ nm. The lattice spacing and depth are $a = \sqrt{3}\,\lambda_L/2$ and $V_L = 8E_r$, respectively, where $E_r = h^2/8ma^2 = h \times 3.1$ kHz (h is the Planck constant). The trapping frequencies of the overall harmonic potential were estimated to be $(\omega_x, \omega_y, \omega_z) \approx 2\pi \times (41, 61, 130)$ Hz. After loading the atoms in the lattice potential, the fractional population of the p orbital was about 3%. Shaking of the lattice potential is implemented by sinusoidally modulating the frequency difference $\delta\omega_L$ between the two lattice laser beams as $\delta\omega_L(t) = A\sin(\omega t + \varphi)$, which results in lattice site vibrations with amplitude $d = \frac{A}{2\pi\omega}a$ [figure 2(a)].

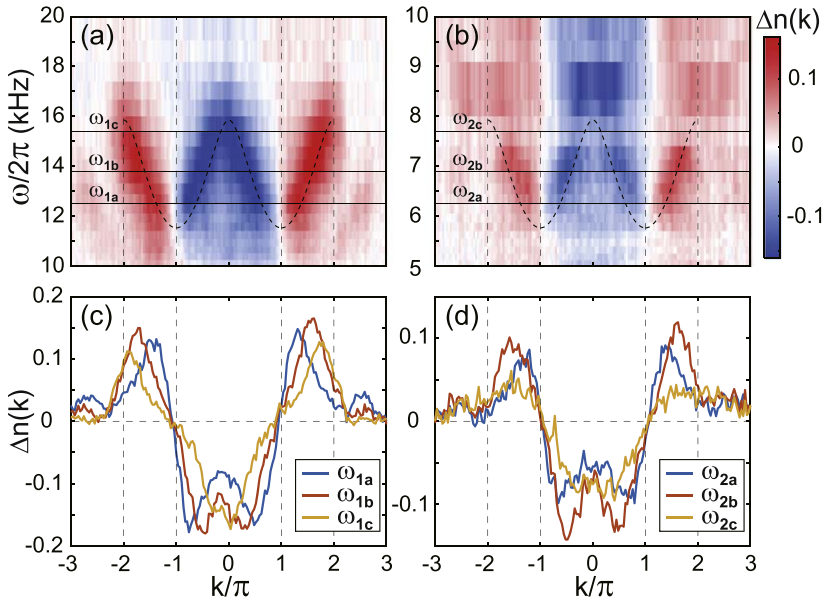

Figure 3. Shaking spectroscopy of fermionic atoms in an optical lattice. (a), (b) Spectra of the momentum distribution change $\Delta n(k)$ as a function of the driving frequency ω. The driving amplitude $A/2\pi = 2$ kHz in (a) and 4 kHz in (b). The dashed lines in (a) and (b) indicate the one-photon and two-photon resonance conditions, i.e. $\omega = \omega_{sp}(q)$ and $2\omega = \omega_{sp}(q)$, respectively[1]. (c), (d) Spectral profiles of $\Delta n(k)$ at various ω, indicated by the horizontal lines in (a) and (b).

4.2. Shaking spectroscopy

We first investigate the resonance condition for inter-obital coupling by measuring the momentum distribution $n(k)$ of the atoms as a function of the driving frequency ω. After preparing the atoms in the s band of the static lattice, we suddenly apply the periodic driving over 20 cycles, which is longer than the dephasing time of the system, and we measure $n(k)$ by taking an absorption image of the atoms after a band mapping protocol [40] and a subsequent time of flight. In the band mapping, quasimomentum states are transformed onto the corresponding real momentum states in free space by slowly ramping down the lattice potential, and $n(k)$ shows the quasimomentum distribution of the atoms in the s band for $|k| < \pi$ with $k = q$ and that in the p band for $\pi < |k| < 2\pi$ with $k = q - \mathrm{sgn}(q) \times (2\pi)$, where k is expressed in units of a^{-1}.

In figure 3, we display the measurement result of the momentum distribution change, $\Delta n(k)$, from that of the non-driven sample as a function of ω. Here $n(k)$ is normalized as $\int n(k)\mathrm{d}k = 1$. A strong spectral signal is observed in the range $\omega/2\pi = 11 \sim 17$ kHz [figure 3(a)]. The spectral peak position follows the one-photon resonance condition $\omega = \omega_{sp}(q) \approx [\epsilon_{sp} - 4t_r \cos(q)]/\hbar$, where $\{\epsilon_{sp},\ t_r\}/h = \{13.4,\ -0.54\}$ kHz for our lattice parameters. The two-photon s–p coupling is observed in the corresponding half-frequency range $\omega/2\pi = 5.5 \sim 8$ kHz (figure 3(b)), where the spectral structure appears consistent with the resonance condition of $2\omega = \omega_{sp}(q)$. In comparison with the one-photon resonance case in figure 3(c), it is noticeable that the signal strength is suppressed at $2\omega \sim \omega_{sp}(0)$ and $2\omega \sim \omega_{sp}(\pm\pi)$, much weaker than that at $2\omega \sim \omega_{sp}(\pm\pi/2)$ (figure 3(d)). The suppression is consistent with the q-dependence of the transverse field amplitude of $\boldsymbol{h}_2$, $h_{2,\rho}(q) \propto \sin(q)$, which determines the coupling strength between the two orbital-momentum states, $|q,\ s\rangle$ and $|q,\ p\rangle$.

In the frequency range of $\omega/2\pi = 11 \sim 14$ kHz and $\omega/2\pi \approx 8.5$ kHz, we observe substantial population transfer to the high-momentum region of $|k| > 2\pi$, which result from the two-photon and three-photon couplings between the s and d orbitals, respectively. In the effort to realize an effective two-leg ladder system, coupling to higher orbitals from the s and p orbitals could be detrimental, if its magnitude is not negligible to that of the s–p inter-orbital coupling. In the two-photon resonance condition with $\Delta_2 = 0$, which is of our main interest in this work, the atom loss rate out of the s–p ladder system was measured to be $\approx 0.17 t_d$ for $A/2\pi = 8$ kHz ($t_d/h = 0.4$ kHz), justifying the effective two-band description of the shaken lattice system. In numerical simulations of an atom in the 1D shaken lattice potential, the atom loss rate due to the higher-band coupling was estimated to be $0.08 t_d$, which is less than a half of the experimentally measured value. Further experimental optimization might help reduce the loss rate, such as phase stabilization of the lattice laser beams and transverse confinement of atoms with additional yz lattices beams. It is worth noting that atom–atom

[1] The long-range hoppings in the p band were included in the calculation of $\omega_{sp}(q)$.

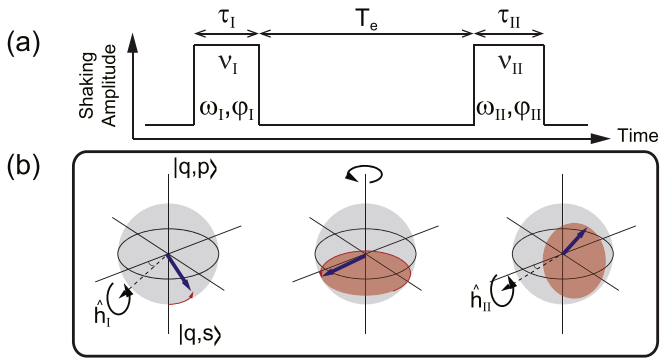

Figure 4. Schematic of Ramsey interferometry using two separate pulses of lattice shaking. (a) Schematic of the lattice shaking sequence and (b) the pseudo-spin evolution on the Bloch sphere for the quasimomentum q state. $\hat{\boldsymbol{h}}_{\mathrm{I(II)}}$ indicates the direction of $\boldsymbol{h}$ for the first (second) shaking pulse. The orange disk denotes the precession plane of the pseudo-spin during the intermittent period.

interactions, which are present in our spin-balanced sample, can be a source of heating and atom loss in a periodically driven optical lattice system [41].

4.3. Ramsey interferometry

In the shaking spectroscopy, the dispersion curve of $\omega_{sp}(q)$ was measured for the two-photon resonant coupling and it confirms the axial component of $\boldsymbol{h}_2$ is given by $h_{2,z} = \Delta_2 - 2t_r\cos(q)$. For verifying the winding stucture of $\boldsymbol{h}_2(q)$, therefore, it would be sufficient to demonstrate the asymmetric property of its transverse component, $h_{2,\rho}(-q) = -h_{2,\rho}(q)$.

As a means to probe the asymmetric property of $h_{2,\rho}(q)$, we employ a Ramsey interferometry scheme, where two separate pulses of resonant lattice shaking are applied with a variable time interval T_e. The lattice shaking sequence is described in figure 4(a), where the frequency modulations are set as $\delta\omega(t) = A_{\mathrm{I}}\sin(\omega_{\mathrm{I}}t + \varphi_{\mathrm{I}})$ for the first pulse in $0 < t < \tau_{\mathrm{I}}$ and as $\delta\omega(t) = A_{\mathrm{II}}\sin(\omega_{\mathrm{II}}t' + \varphi_{\mathrm{II}})$ with $t' = t - (\tau_{\mathrm{I}} + T_e)$ for the second pulse in $0 < t' < \tau_{\mathrm{II}}$. Here, $\omega_{\mathrm{I(II)}} = \omega_{sp}^0/\nu_{\mathrm{I(II)}}$ ($\omega_{sp}^0/2\pi = 13.4$ kHz) with $\nu_{\mathrm{I(II)}}$=1 or 2 so that during the first (second) pulse duration, the $\nu_{\mathrm{I(II)}}$-photon resonant coupling is generated in the lattice system. As shown in section 3, in a rotating frame with frequency $\omega_{sp}^0 = \nu_{\mathrm{I(II)}}\omega_{\mathrm{I(II)}}$, the effective Bloch Hamiltonian of the resonantly shaken lattice system is given by $H_q(t) = -2\bar{t}_r\cos(q)\mathbb{I} + \boldsymbol{h}(q,\,t)\cdot\boldsymbol{\sigma}$ with $\boldsymbol{h}(q,\,t) = -2t_r\cos(q)\sigma_z + h_\rho(q,\,t)[\cos(\theta(t)\sigma_x + \sin(\theta(t)\sigma_y]$. During the Ramsey interferometry sequence, the transverse component of $\boldsymbol{h}(q,\,t)$ is dynamically controlled with the lattice shaking parameters, $\{\nu_{\mathrm{I(II)}},\,A_{\mathrm{I(II)}},\,\varphi_{\mathrm{I(II)}}\}$.

For an atom initially prepared in the $|q,\,s\rangle$ state, its final state after the Ramsey interferomentry sequence is given by

$$\begin{pmatrix} c_p(q) \\ c_s(q) \end{pmatrix} = R_{\hat{\boldsymbol{h}}_{\mathrm{II}}(q)}(\xi_{\mathrm{II}})R_{\hat{\boldsymbol{z}}}(h_z(q)\,T_e/\hbar)R_{\hat{\boldsymbol{h}}_{\mathrm{I}}(q)}(\xi_{\mathrm{I}})\begin{pmatrix} 0 \\ 1 \end{pmatrix}, \tag{8}$$

where $\boldsymbol{h}_{\mathrm{I(II)}}$ is the $\boldsymbol{h}$ vector in the first (second) lattice shaking and $\xi_{\mathrm{I(II)}} = |\boldsymbol{h}_{\mathrm{I(II)}}|\tau_{\mathrm{I(II)}}/\hbar$. Here the global phase factor arising from the term of $-2\bar{t}_r\cos(q)\mathbb{I}$ in H_q is ignored under a proper gauge transformation. $R_{\hat{\boldsymbol{n}}}(\xi)$ represents a rotation around the $\hat{\boldsymbol{n}}$ axis by ξ on the Bloch sphere formed by $|q,\,p\rangle$ and $|q,\,s\rangle$, and thus, the system's overall evolution is described as a composition of three sequential rotations which correspond to the time evolutions in the first pulse, the intermediate period, and the second pulse, respectively [figure 4(b)]. As the time T_e of the intermediate period increases, the atom population in the $|q,\,p\rangle$ state, $n_p(q) = |c_p(q)|^2$ would show oscillations, and its oscillation amplitude and phases can reveal the geometric relation between $\boldsymbol{h}_{\mathrm{I}}(q)$ and $\boldsymbol{h}_{\mathrm{II}}(q)$.

In our experiment, we examine two cases of $(\nu_{\mathrm{I}}, \nu_{\mathrm{II}}) = (1, 1)$ and $(2, 1)$ with $\varphi_{\mathrm{I(II)}} = 0$ and $\tau_{\mathrm{I(II)}} = 2\pi/\omega_{\mathrm{I(II)}}$. We measure the momentum distribution $n(k)$ after applying the two pulses of lattice shaking with increasing T_e. In figure 5(a), the measurement result for the $(\nu_{\mathrm{I}},\,\nu_{\mathrm{II}}) = (1,\,1)$ case is presented, where the shaking amplitude is set to be $A_{\mathrm{I(II)}}/2\pi = 5$ kHz to obtain $\xi_{\mathrm{I(II)}} = \pi/4$ for $q = \pm 0.7\pi$. The population oscillations with increasing T_e are clearly observed for each q and the oscillation frequency is found to be in good quantitative agreement with $\omega_{sp}(q)$ (figure 7(a)). Next, the measurement result for $(\nu_{\mathrm{I}}, \nu_{\mathrm{II}}) = (2, 1)$ is presented in figure 5(b). In the measurement, the driving amplitude for the first pulse ($\nu_{\mathrm{I}} = 2$) is changed to $A_{\mathrm{I}}/2\pi = 8$ kHz to keep $\xi_{\mathrm{I}} = \pi/4$ for $q = \pm 0.7\pi$, whereas that for the second pulse ($\nu_{\mathrm{II}} = 1$) is the same as in the previous $(\nu_{\mathrm{I}}, \nu_{\mathrm{II}}) = (1, 1)$ measurement. Remarkably, we observe that the Ramsey signals exhibit an asymmetric fringe pattern with respect to $k = 0$, which is in stark contrast to the $(\nu_{\mathrm{I}}, \nu_{\mathrm{II}}) = (1, 1)$ case where the Ramsey signals are mirror-symmetric. Based on the fact that the transverse component of $\boldsymbol{h}_{\mathrm{II}}(q)$ with $\nu_{\mathrm{II}} = 1$ is uniform over the BZ

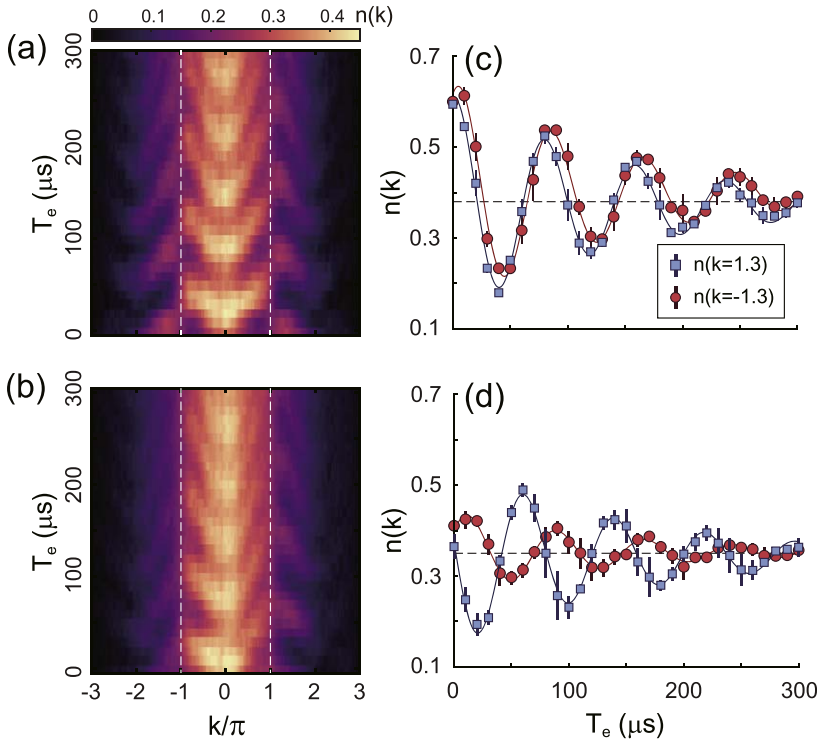

Figure 5. Momentum-resolved Ramsey interferometry signal. Momentum distribution $n(k)$ as a function of T_e for (a) $(\nu_{\rm I}, \nu_{\rm II}) = (1, 1)$ and (b) (2, 1), where $\varphi_{\rm I(II)} = 0$ and $\tau_{\rm I(II)} = 2\pi/\omega_{\rm I(II)}$. (c), (d) $n(k)$ at $k = \pm 1.3\pi$ as a function of T_e in (a) and (b), respectively. The solid lines are the damped sinusoidal function fits to the data. Each data point was obtained from seven measurements and its error bar indicates their standard deviation.

[equation (7)], the observed asymmetric fringe signals indicate that the transverse component of $\boldsymbol{h}_{\rm I}(q)$ with $\nu_{\rm I} = 2$ has opposite directions for $q > 0$ and $q < 0$, i.e. $h_{2,\rho}(-q) = -h_{2,\rho}(q)$, thus corroborating the winding structure of $\boldsymbol{h}_2(q)$.

In figures 5(c) and (d), we display the population $n(k)$ at $k = \pm 1.3\pi$, corresponding to $n_p(q = \mp 0.7\pi)$, as a function of T_e for the $(\nu_{\rm I}, \nu_{\rm II}) = (1, 1)$ and (2, 1) cases, respectively. The population shows damped oscillations with increasing T_e and the damping might be attributed to atom–atom interactions and/or the spatial inhomogeneity of the trapped sample. From the damped sinuoidal functions fit to the data, we measured the phase difference between the two oscillation curves to be 0.10π for $(\nu_{\rm I}, \nu_{\rm II}) = (1, 1)$ and 0.77π for $(\nu_{\rm I}, \nu_{\rm II}) = (2, 1)$, which are slightly different from the expected values of 0 and π, respectively. We attribute such a small deviation to the off-resonant coupling effect, which is neglected in our model description and will be further discussed in the next section.

As a further comparison of the $(\nu_{\rm I}, \nu_{\rm II}) = (1, 1)$ and (2, 1) cases, we also examine the dependence of the Ramsey signal on the driving phases $\varphi_{\rm I}$ and $\varphi_{\rm II}$ by measuring $n(k = \pm 1.3\pi)$ as a function of $\varphi_{\rm I}$ and $\varphi_{\rm II}$ with a fixed evolution time $T_e = 100\ \mu$s (figure 6). For $(\nu_{\rm I}, \nu_{\rm II}) = (1, 1)$, the two populations at $k = \pm 1.3\pi$ oscillate in phase with period of 2π in both $\varphi_{\rm I}$ and $\varphi_{\rm II}$. In contrast, for $(\nu_{\rm I}, \nu_{\rm II}) = (2, 1)$, they show out-of-phase oscillations with a different period of π in $\varphi_{\rm I}$ and 2π in $\varphi_{\rm II}$. This observation is consistent with the different φ-dependence of $\hat{\boldsymbol{\rho}}_1$ and $\hat{\boldsymbol{\rho}}_2$ in equation (7). The π periodicity of the Ramsey signal with increasing $\varphi_{\rm I}$ for $\nu_{\rm I} = 2$ is a direct consequence of that the inter-orbital coupling is generated via two-photon process.

5. Discussions

5.1. Off-resonance coupling effect

In the model description of the resonantly shaken lattice system, we consider only the effects of the resonant coupling between the *s* and *p* orbitals. Although the model is efficient in capturing the essential topological features of the system, its improvement, in particular, by including the off-resonant inter-orbital coupling effects would be necessarily desirable for further development of the ladder system. To evaluate the limitations of the current model, we make a quantitative comparison between the experimental results in the Ramsey interferometry measurement and the prediction from the model. In figure 7, we characterize the Ramsey interferometry data presented in figures 5(a) and (b) with the oscillating frequency $\omega_f(k)$ and the phase $\phi(k)$,

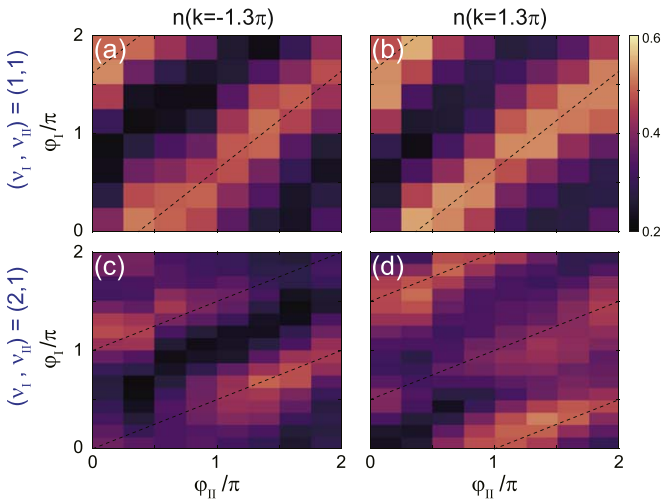

Figure 6. Driving phase dependence of the Ramsey fringe signal. Atomic densities $n(k)$ measured at (a), (c) $k = -1.3\pi$ and (b), (d) $k = 1.3\pi$ as functions of the driving phases $\varphi_{\rm I}$ and $\varphi_{\rm II}$ for $T_e = 100$ μs. $(\nu_{\rm I}, \nu_{\rm II}) = (1, 1)$ in (a), (b) and (2, 1) in (c), (d). The experimental conditions are the same as those in figure 5. The dashed lines are guides to the eyes, indicating the maxima of the Ramsey fringes. In the case of $(\nu_{\rm I}, \nu_{\rm II}) = (2, 1)$, the fringe signal shows π-periodicity with increasing $\varphi_{\rm I}$.

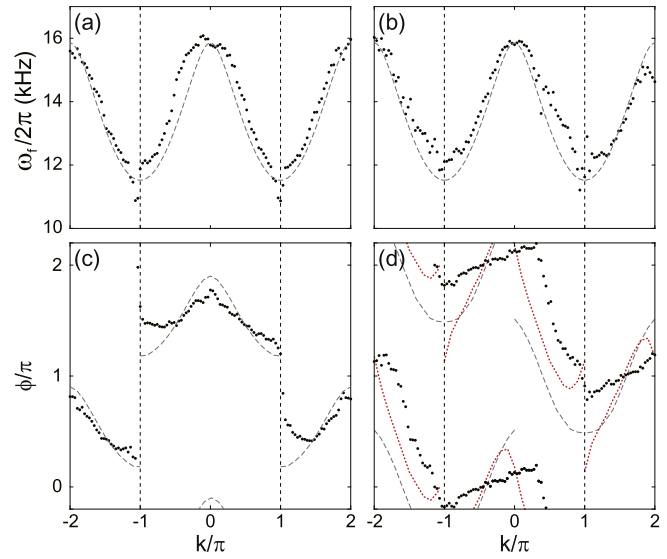

Figure 7. Characterization of the Ramsey fringe signals. The oscillation frequency $\omega_f(k)$ and phase $\phi(k)$ were determined from a damped sinusoidal function fit to the experimental data for each k. (a) and (c) for the data with $(\nu_{\rm I}, \nu_{\rm II}) = (1, 1)$ in figures 5(a), and (b) and (d) for the data with $(\nu_{\rm I}, \nu_{\rm II}) = (2, 1)$ in figure 5(b). The grey dashed lines indicate the model prediction calculated from equation (8). The red dots in (d) show the numerical result for the case where a uniform transverse vector of $(\max[h_\rho]/3)\hat{\boldsymbol{x}}$ is added to $\boldsymbol{h}_{\rm I}$ (see the text for details).

where $\{\omega_f(k), \phi(k)\}$ are determined from a damped sinusoidal function fit to the fringe signal $n(T_e; k)$ at each k. In the $(\nu_{\rm I}, \nu_{\rm II}) = (1, 1)$ case, we find that the measured $\{\omega_f(k), \phi(k)\}$ are well described by the model [figures 7(a) and (c)]. Here, the model prediction was numerically obtained by calculating equation (8) for the experimental conditions. On the other hand, in the $(\nu_{\rm I}, \nu_{\rm II}) = (2, 1)$ case, we observe that the measured oscillation phase $\phi(k)$ shows a quantitatively non-negligible deviation from the model prediction [figure 7(d)]. The deviation is pronounced near $k = 0$ and $\pm\pi$. These momentum regions are where the two-photon resonant coupling is weak for $h_{2,\rho}(q) \propto \sin(q)$ so that it is not only technically difficult to precisely determine ϕ but also likely to be sensitive to any off-resonant coupling effect.

In the two-photon resonance condition, the dominant off-resonant coupling must arise from the one-photon inter-orbital transition process. We speculate that its effect might be approximated to direct *leakage* links between the two legs, and then represented by a uniform transverse component in $\boldsymbol{h}$ as observed in the case of one-photon resonant coupling. To test the possibility, we recalculate equation (8) for the $(\nu_{\rm I}, \nu_{\rm II}) = (2, 1)$

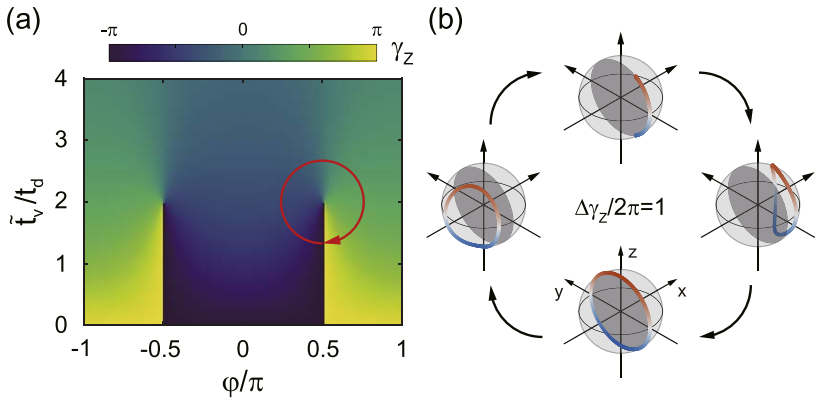

Figure 8. Topological charge pumping in the Creutz ladder. (a) Zak phase γ_Z in the plane of $\tilde{t}_v/t_d$ and φ. The critical points are located at $\{\tilde{t}_v/t_d, \varphi\} = \{2, \pm\pi/2\}$. Along the path encircling one of the critical points, γ_Z continuously changes by 2π. (b) Evolution cycle of the pseudo-spin trajectory of the ground band on the Bloch sphere as the system adiabatically moves along the red encircling path in (a). The trajectory line covers the whole Bloch sphere in each cycle, resulting in one lattice site shift of atoms in the Creutz ladder.

experiment with adding a transverse field of $h_x\hat{\boldsymbol{x}}$ to $\boldsymbol{h}_1$ for the first pulse period. We observe that the numerical result evolves somewhat closely to the exeprimental data when h_x increases to $\max[h_\rho]/3$ [figure 7(d)], supporting the leakage-link picture for the off-resonant coupling effect. The presence of such leakage links has an important implication that depending on the complex amplitude of the leakage links, $\boldsymbol{h}$ might not be confined in a plane so that its winding number would be ill-defined. The off-resonant coupling effects, including those from the coupling to higher orbitals, warrant further theoretical and experimental investigations in future study.

5.2. Shaking with two resonant frequencies

The observation that one- and two-photon resonant couplings bring about the distinctive effects of direct and cross inter-leg links, respectively, prompts us to discuss an extension of the inter-leg link control in the ladder by using both types of resonant couplings. Specifically, we consider a situation in which the lattice shaking is applied as $\delta\omega_L(t) = A\sin(\omega t) + \tilde{A}\sin(2\omega t + \varphi)$ with $\Delta_2 = 0$. Here, together with the ω driving generating two-photon resonant coupling, the 2ω driving provides one-photon resonant coupling. We find that the inter-orbital coupling effects of the two drivings appears additive in the effective Hamiltonian at the same level of approximation used in equation (7) (see appendix B), giving

$$\boldsymbol{h}(q) = \tilde{t}_v\hat{\boldsymbol{\rho}}_1(\varphi) + 2t_d\sin(q)\hat{\boldsymbol{y}} - 2t_r\cos(q)\hat{\boldsymbol{z}},$$

with $\tilde{t}_v = (\tilde{A}/A)t_v$. This suggests that the direct inter-leg links can be generated independently in the Creutz ladder by simply adding a 2ω driving; furthermore, its complex amplitude can be controlled with the driving parameters $\tilde{A}$ and φ. Even with the off-resonant coupling effects discussed in the previous subsection, this two-tone driving method would provide a flexible way to control the inter-leg links of the Creutz ladder system.

The extended control of the inter-leg links will enable to explore many interesting aspects of the topological ladder system. First of all, the topological phase transition of the Creutz ladder can be studied in a controlled manner, which occurs at $\{\tilde{t}_v, \varphi\}_c = \{2t_d, \pm\pi/2\}$, accompanied by the band gap closing at $q = \pm\pi/2$ and a sudden change of the winding number of $\boldsymbol{h}(q)$. Anomalous scaling of defect formation was predicted for the phase transition dynamics due to the topological properties of the system [25]. Equipped with the dynamic control of the inter-leg links, we can also envisage a realization of a topological charge pump in the Creutz ladder [42]. For example, when the direct link parameters $\{\tilde{t}_v, \varphi\}$ are controlled to adiabatically encircle one of the critical points in the parameter space, the Zak phase γ_Z [47] continuously changes by 2π per cycle (figure 8), which would result in one lattice site shift of atoms in the ladder.

6. Conclusion

We have demonstrated the realization of the Creutz ladder in a periodically shaken 1D optical lattice via two-photon resonant coupling. The topological structure of the Creutz ladder was characterized with the winding structure of $\boldsymbol{h}_2(q)$ in the BZ. By the shaking spectroscopy, the longitudinal component of $\boldsymbol{h}_2$ was directly measured as $h_z = -2t_r\cos(q)$, and using the Ramsey interferometry, the asymmetric relation of its transverse component, $h_{2,\rho}(-q) = -h_{2,\rho}(q)$, was demonstrated. From the observation that one- and two-photon resonant couplings generate direct and diagonal inter-leg links, respectively, in the ladder system, we suggested

the two-tone driving method of simultaneously exploiting both resonant couplings, which would allow the controlled study of the topological phase transition dynamics and the realization of a topological charge pump. As another extension of this work, topological flat band engineering may be pursued with the Creutz ladder system, which would provide interesting opportunities for observing possible emergence of correlated topological phases [43, 44]. In interacting two-leg ladder systems, many correlated topological phases and associated edge states were theoretically discussed [27–31]. Finally, we also expect that the two-photon resonant coupling method can be readily applied to 2D optical lattice systems, providing an alternative route to investigate anomalous quantum Hall states [45, 46].

Acknowledgments

We thank Wei Zheng and Hui Zhai for helpful discussions. This work was supported by the Institute for Basic Science in Korea (Grant No. IBS-R009-D1) and the National Research Foundation of Korea (Grants No. NRF-2018R1A2B3003373, and No. 2014-H1A8A1021987).

Appendix A. Two-band model description

In the two-band tight binding approximation, the Hamiltonian of the lattice system is given by

$$H = \sum_j \Psi_j^\dagger K(t) \Psi_j - \sum_j [\Psi_j^\dagger J(t) \Psi_{j+1} + \text{h.c.}]. \tag{A.1}$$

In terms of the identity and Pauli matrices $\{\mathbb{I}, \sigma_x, \sigma_y, \sigma_z\}$, the matrices $K(t)$ and $J(t)$ are expressed as

$$\begin{aligned} K(t) &= \bar{\epsilon}\mathbb{I} + \frac{\epsilon_{sp}}{2}\sigma_z + h_0^{sp}\sin(\omega t + \varphi)\sigma_y \\ J(t) &= [\bar{t}_r - \mathrm{i}\bar{h}_1 \sin(\omega t + \varphi)]\mathbb{I} + [t_r - \mathrm{i}h_1 \sin(\omega t + \varphi)]\sigma_z - h_1^{sp}\sin(\omega t + \varphi)\sigma_y \end{aligned} \tag{A.2}$$

with $\bar{\epsilon} = \frac{\epsilon_p + \epsilon_s}{2}$, $\epsilon_{sp} = \epsilon_p - \epsilon_s$, $\bar{t}_r = \frac{t_p + t_s}{2}$, $t_r = \frac{t_p - t_s}{2}$, $\bar{h}_1 = \frac{h_1^{pp} + h_1^{ss}}{2}$, and $h_1 = \frac{h_1^{pp} - h_1^{ss}}{2}$.

To investigate the effects of the ν-photon inter-orbital resonant coupling, we obtain the Hamiltonian H' in a rotating reference frame with frequency $\nu\omega$, taking a unitary transformation of

$$U_2(t) = \sum_j [\mathrm{e}^{-\mathrm{i}\frac{\nu\omega}{2}t} c_{j,p}^\dagger c_{j,p} + \mathrm{e}^{\mathrm{i}\frac{\nu\omega}{2}t} c_{j,s}^\dagger c_{j,s}]. \tag{A.3}$$

Then, $K(t)$ and $J(t)$ are transformed to, respectively

$$\begin{aligned} K'(t) &= \Delta_\nu \sigma_z + h_0^{sp}\sin(\omega t + \varphi) R_{\hat{z}}(-\nu\omega t)\sigma_y \\ J'(t) &= [\bar{t}_r - \mathrm{i}\bar{h}_1 \sin(\omega t + \varphi)]\mathbb{I} + [t_r - \mathrm{i}h_1 \sin(\omega t + \varphi)]\sigma_z - h_1^{sp}\sin(\omega t + \varphi) R_{\hat{z}}(-\nu\omega t)\sigma_y, \end{aligned} \tag{A.4}$$

where $\Delta_\nu = (\epsilon_{sp} - \nu\hbar\omega)/2$ and $R_{\hat{z}}(\theta) = \exp(-\mathrm{i}\theta\sigma_z)$. Here we ignore the energy offset of $\bar{\epsilon}\mathbb{I}$ in $K(t)$.

A.1. Effective Hamiltonian for $\nu = 1$

Using a high frequency expansion method up to second order processes [37], the effective Floquet Hamiltonian of the periodically driven system is obtained as

$$H_{\text{eff}}^{(\nu)} = H_0 + \sum_{n=1}^{\infty} \frac{[H_n, H_{-n}]}{n\hbar\omega}, \tag{A.5}$$

where H_n is the $n\omega$ Fourier component of the original time-periodic Hamiltonian $\hat{H}'(t)$, such that

$$H'(t) = H_0 + \sum_{n\neq 0} H_n \mathrm{e}^{\mathrm{i}n\omega t}. \tag{A.6}$$

In the case of $\nu = 1$, from (A.4)

$$\begin{aligned} H_0 &= \sum_j \Psi_j^\dagger \left[\Delta_1\sigma_z + \frac{h_0^{sp}}{2} R_{\hat{z}}(\varphi)\sigma_x\right]\Psi_j + \sum_j \left\{\Psi_j^\dagger \left[-\bar{t}_r\mathbb{I} - t_r\sigma_z + \frac{h_1^{sp}}{2} R_{\hat{z}}(\varphi)\sigma_x\right]\Psi_{j+1} + \text{h.c.}\right\} \\ H_1 &= \sum_j \left\{\Psi_j^\dagger \left[\frac{\mathrm{e}^{\mathrm{i}\varphi}}{2}(\bar{h}_1\mathbb{I} + h_1\sigma_z)\right]\Psi_{j+1} + \Psi_{j+1}^\dagger \left[-\frac{\mathrm{e}^{\mathrm{i}\varphi}}{2}(\bar{h}_1\mathbb{I} + h_1\sigma_z)\right]\Psi_j\right\} \\ H_2 &= \sum_j \Psi_j^\dagger \left[-\frac{h_0^{sp}}{2}\mathrm{e}^{\mathrm{i}\varphi}\sigma^+\right]\Psi_j + \sum_j \left\{\Psi_j^\dagger \left[\frac{-h_1^{sp}}{2}\mathrm{e}^{\mathrm{i}\varphi}\sigma^+\right]\Psi_{j+1} + \Psi_{j+1}^\dagger \left[\frac{-h_1^{sp}}{2}\mathrm{e}^{\mathrm{i}\varphi}\sigma^+\right]\Psi_j\right\} \end{aligned} \tag{A.7}$$

and $H_{-n} = H_n^\dagger$, where $\sigma^\pm = (\sigma_x \pm \mathrm{i}\sigma_y)/2$. Then

$$H_{\mathrm{eff}}^{(1)} = \sum_j \Psi_j^\dagger \left[\left(\Delta_1 + \frac{(h_0^{sp})^2 + (h_1^{sp})^2}{8\hbar\omega} \right) \sigma_z + \frac{h_0^{sp}}{2} R_{\hat{z}}(\varphi)\sigma_x \right] \Psi_j + \sum_j \left\{ \Psi_j^\dagger \left[-\bar{t}_r \mathbb{I} + \left(\frac{h_0^{sp} h_1^{sp}}{4\hbar\omega} - t_r \right) \sigma_z + \frac{h_1^{sp}}{2} R_{\hat{z}}(\varphi)\sigma_x \right] \Psi_{j+1} + \Psi_j^\dagger \left[\frac{(h_1^{sp})^2}{8\hbar\omega} \sigma_z \right] \Psi_{j+2} + \mathrm{h.c.} \right\}. \tag{A.8}$$

When $\hbar\omega \gg h_0^{sp} \gg h_1^{sp}$, the effective Hamiltonian is approximated as

$$H_{\mathrm{eff}}^{(1)} \approx \sum_j \Psi_j^\dagger [\Delta_1 \sigma_z + t_v R_{\hat{z}}(\varphi)\sigma_x] \Psi_j - \sum_j \{ \Psi_j^\dagger (\bar{t}_r \mathbb{I} + t_r \sigma_z) \Psi_{j+1} + \mathrm{h.c.} \} \tag{A.9}$$

with $t_v = h_0^{sp}/2$. The Bloch Hamiltonian is given by

$$H_q^{(1)} = -2\bar{t}_r \cos(q)\mathbb{I} + \boldsymbol{h}_1(q) \cdot \boldsymbol{\sigma}$$

with

$$\begin{aligned} \boldsymbol{h}_1(q) &= t_v \hat{\boldsymbol{\rho}}_1 + [\Delta_1 - 2t_r \cos(q)]\hat{\boldsymbol{z}} \\ \hat{\boldsymbol{\rho}}_1 &= \cos(\varphi)\hat{\boldsymbol{x}} + \sin(\varphi)\hat{\boldsymbol{y}}, \end{aligned} \tag{A.10}$$

where q is the quasimomentum normalized in units of a^{-1}.

A.2. Effective Hamiltonian for $\nu = 2$

In the case of $\nu = 2$

$$\begin{aligned} H_0 &= \sum_j \Psi_j^\dagger (\Delta_2 \sigma_z) \Psi_j - \sum_j [\Psi_j^\dagger (\bar{t}_r \mathbb{I} + t_r \sigma_z) \Psi_{j+1} + \mathrm{h.c.}] \\ H_1 &= \sum_j \Psi_j^\dagger \left[\frac{h_0^{sp}}{2} \mathrm{e}^{-\mathrm{i}\varphi\sigma^+} \right] \Psi_j + \sum_j \{ \Psi_j^\dagger \left[\frac{h_1^{sp}}{2} \mathrm{e}^{-\mathrm{i}\varphi\sigma^+} + \frac{\mathrm{e}^{\mathrm{i}\varphi}}{2} (\bar{h}_1 \mathbb{I} + h_1 \sigma_z) \right] \Psi_{j+1} \\ &\quad + \Psi_{j+1}^\dagger \left[\frac{h_1^{sp}}{2} \mathrm{e}^{-\mathrm{i}\varphi\sigma^+} - \frac{\mathrm{e}^{\mathrm{i}\varphi}}{2} (\bar{h}_1 \mathbb{I} + h_1 \sigma_z) \right] \Psi_j \} \\ H_3 &= \sum_j \Psi_j^\dagger \left[-\frac{h_0^{sp}}{2} \mathrm{e}^{\mathrm{i}\varphi\sigma^+} \right] \Psi_j + \sum_j \left\{ \Psi_j^\dagger \left[\frac{-h_1^{sp}}{2} \mathrm{e}^{\mathrm{i}\varphi\sigma^+} \right] \Psi_{j+1} + \Psi_{j+1}^\dagger \left[\frac{-h_1^{sp}}{2} \mathrm{e}^{\mathrm{i}\varphi\sigma^+} \right] \Psi_j \right\}, \end{aligned} \tag{A.11}$$

giving

$$\begin{aligned} H_{\mathrm{eff}}^{(2)} &= \sum_j \Psi_j^\dagger \left[\left(\Delta_2 + \frac{(h_0^{sp})^2 + (h_1^{sp})^2}{3\hbar\omega} \right) \sigma_z - \frac{h_1^{sp} h_1}{2\hbar\omega} R_{\hat{z}}(2\varphi)\sigma_x \right] \Psi_j \\ &\quad + \sum_j \{ \Psi_j^\dagger \left[-\bar{t}_r \mathbb{I} + \left(\frac{2h_0^{sp} h_1^{sp}}{3\hbar\omega} - t_r \right) \sigma_z + \frac{h_0^{sp} h_1}{2\hbar\omega} R_{\hat{z}}(2\varphi)\mathrm{i}\sigma_y \right] \Psi_{j+1} \\ &\quad + \Psi_j^\dagger \left[\frac{(h_1^{sp})^2}{3\hbar\omega} \sigma_z + \frac{h_1^{sp} h_1}{2\hbar\omega} R_{\hat{z}}(2\varphi)\mathrm{i}\sigma_y \right] \Psi_{j+2} + \mathrm{h.c.} \}. \end{aligned} \tag{A.12}$$

With $\hbar\omega \gg h_0^{sp} > h_1 > h_1^{sp}$, $H_{\mathrm{eff}}^{(2)}$ is approximated as

$$H_{\mathrm{eff}}^{(2)} \approx \sum_j \Psi_j^\dagger (\Delta_2 \sigma_z) \Psi_j - \sum_j \{ \Psi_j^\dagger [\bar{t}_r \mathbb{I} + t_r \sigma_z - t_d R_{\hat{z}}(2\varphi)\mathrm{i}\sigma_y] \Psi_{j+1} + \mathrm{h.c.} \} \tag{A.13}$$

with $t_d = h_0^{sp} h_1/(2\hbar\omega)$. Here, we ignore the ac Stark shift, $\delta_2^{ac} \approx \frac{(h_0^{sp})^2}{3\hbar\omega}$, in the orbital energy, which is comparable to t_d in magnitude but much smaller than t_r in the experiment. The Bloch Hamiltonian is given by

$$H_q^{(2)} = -2\bar{t}_r \cos(q)\mathbb{I} + \boldsymbol{h}_2(q) \cdot \boldsymbol{\sigma}$$

with

$$\begin{aligned} \boldsymbol{h}_2(q) &= 2t_d \sin(q) \hat{\boldsymbol{\rho}}_2 + [\Delta_2 - 2t_r \cos(q)]\hat{\boldsymbol{z}} \\ \hat{\boldsymbol{\rho}}_2 &= -\sin(2\varphi)\hat{\boldsymbol{x}} + \cos(2\varphi)\hat{\boldsymbol{y}}. \end{aligned} \tag{A.14}$$

For our experimental condition, h_0^{sp}: h_1: h_1^{sp} = 6.4: 1.7: 0.3 and $h_0^{sp}/h < 1.3$ kHz, whereas $\omega/2\pi = 13.7$ or 6.8 kHz, and $t_r/h = 0.54$ kHz, justifying the approximation taken in (A.9) and (A.13).

Appendix B. Two-tone driving scheme

In this section, we consider the situation where the optical lattice system is driven with

$$\delta\omega(t) = A\sin(\omega t) + \tilde{A}\sin(2\omega t + \varphi). \tag{B.1}$$

Following the derivation in appendix A, we obtain the Hamiltonian in the comoving frame as

$$H = \frac{p_x^2}{2m} + \frac{V_L}{2}\cos(2k_L x) - \mathrm{d}\omega\sin(\omega t)p - 2\tilde{\mathrm{d}}\omega\sin(2\omega t + \varphi)p_x. \tag{B.2}$$

In two-band tight binding approximation, the Hamiltonian $\hat{H}'$ in a rotating reference frame with frequency 2ω is given by

$$H' = \sum_j \{\Psi_j^\dagger K'(t)\Psi_j - (\Psi_j^\dagger J'(t)\Psi_{j+1} + \mathrm{h.c.})\},$$

with

$$\begin{aligned} K'(t) &= \Delta_2\sigma_z + h_0^{sp}\sin(\omega t)R_{\hat{z}}(-2\omega t)\sigma_y + \tilde{h}_0^{sp}\sin(2\omega t + \varphi)R_{\hat{z}}(-2\omega t)\sigma_y, \\ J'(t) &= \bar{t}_r\mathbb{I} + t_r\sigma_z - \mathrm{i}[\bar{h}_1\sin(\omega t) + \tilde{\bar{h}}_1\sin(2\omega t + \varphi)]\mathbb{I} - \mathrm{i}[h_1\sin(\omega t) + \tilde{h}_1\sin(2\omega t + \varphi)]\sigma_z \\ &\quad - h_1^{sp}\sin(\omega t)R_{\hat{z}}(-2\omega t)\sigma_y - \tilde{h}_1^{sp}\sin(2\omega t + \varphi)R_{\hat{z}}(-2\omega t)\sigma_y. \end{aligned} \tag{B.3}$$

The tilde symbol indicates that the elements are derived from the 2ω driving with the amplitude $\tilde{A}$.

The effective Hamiltonian, H_{eff}, of the driven system can be obtained in a same manner shown in Appendix A using the high frequency expansion method. Here, we note that the Fourier components, $H_{\pm1}$ and $H_{\pm3}$ are generated only by the ω driving to have the same forms obtained in (A.11), and $H_{\pm2}$ and $H_{\pm4}$ come only from the 2ω driving, resulting in the same forms of $H_{\pm1}$ and $H_{\pm2}$ in (A.7). Then, (A.5) shows that the effects of the two drivings additively arise in the system, thus leading to

$$H_{\mathrm{eff}} \approx \sum_j \Psi_j^\dagger[\Delta_2\sigma_z + \tilde{t}_v R_{\hat{z}}(\varphi)\sigma_x]\Psi_j - \sum_j[\Psi_j^\dagger(\bar{t}_r\mathbb{I} + t_r\sigma_z - t_d\mathrm{i}\sigma_y)\Psi_{j+1} + \mathrm{h.c.}] \tag{B.4}$$

with $\tilde{t}_v = \tilde{h}_0^{sp}/2$ and $t_d = h_0^{sp}h_1/2\hbar\omega$. Here the same approximations used in (A.9) and (A.13) are applied. Accordingly, in the quasimomentum space, the Bloch Hamiltonian is given by

$$H_q = -2\bar{t}_r\cos(q)\mathbb{I} + \boldsymbol{h}(q)\cdot\boldsymbol{\sigma}$$

with

$$\boldsymbol{h}(q) = \tilde{t}_v\hat{\boldsymbol{\rho}} + 2t_d\sin(q)\hat{\boldsymbol{y}} + [\Delta_2 - 2t_r\cos(q)]\hat{\boldsymbol{z}}\hat{\boldsymbol{\rho}} = \cos(\varphi)\hat{\boldsymbol{x}} + \sin(\varphi)\hat{\boldsymbol{y}}. \tag{B.5}$$

References

[1] Hasan M Z and Kane C L 2010 Colloquium: topological insulators *Rev. Mod. Phys.* **82** 3045
[2] Qi X-L and Zhang S-C 2011 Toplogical insulators and superconductors *Rev. Mod. Phys.* **83** 1057
[3] Goldman N, Budich J C and Zoller P 2016 Topological quantum matter with ultracold gases in optical lattices *Nat. Phys.* **12** 639
[4] Cooper N R, Dalibard J and Spielman I B 2019 Topological bands for ultracold atoms *Rev. Mod. Phys.* **91** 015005
[5] Aidelsburger M, Atala M, Lohse M, Barreiro J T, Paredes B and Bloch I 2013 Realization of the Hofstadter Hamiltonian with ultracold atoms in optical lattices *Phys. Rev. Lett.* **111** 185301
[6] Miyake H, Siviloglou G A, Kennedy C J, Burton W C and Ketterle W 2013 Realizing the Harper Hamiltonian with laser-assisted tunneling in optical lattices *Phys. Rev. Lett.* **111** 185302
[7] Jotzu G, Messer M, Desbuquois R, Lebrat M, Uehlinger U, Greif D and Esslinger T 2014 Experimental realization of the topological Haldane model with ultracold fermions *Nature* **515** 237
[8] Mancini M *et al* 2015 Observation of chiral edge states with neutral fermions in synthetic Hall ribbons *Science* **349** 1510
[9] Stuhl B K, Lu H-I, Aycock L M, Genkina M and Spielman I B 2015 Visualizing edge states with an atomic Bose gas in the quantum Hall regime *Science* **349** 1514
[10] Livi L F *et al* 2016 Synthetic dimensions and spin–orbit coupling with an optical clock transition *Phys. Rev. Lett.* **117** 220401
[11] Kolkowitz S, Bromley S L, Bothwell T, Wall M L, Marti G E, Koller A P, Zhang X, Rey A M and Ye J 2017 Spin-orbit-coupled fermions in an optical lattice clock *Nature* **542** 66
[12] Song B, Zhang L, He C, Poon T F J, Hajiyev E, Zhang S, Liu X-J and Jo G-B 2018 Observation of symmetry-protected topological band with ultracold fermions *Sci. Adv.* **4** eeao4748
[13] Han J H, Kang J H and Shin Y 2019 Band gap closing in a synthetic Hall tube of neutral fermions *Phys. Rev. Lett.* **122** 065303
[14] Kang J H, Han J H and Shin Y 2018 Realization of a cross-linked chiral ladder with neutral fermions in a 1D optical lattice by orbital-momentum coupling *Phys. Rev. Lett.* **121** 150403
[15] Lignier H, Sias C, Ciampini D, Singh Y, Zenesini A, Morsch O and Arimondo E 2007 Dynamical control of matter-wave tunneling in periodic potentials *Phys. Rev. Lett.* **99** 220403
[16] Struck J, Ölschläger C, Le Targat R, Soltan-Panahi P, Eckardt A, Lewenstein M, Windpassinger P and Sengstock K 2011 Quantum simulation of frustrated classical magnetism in triangular optical lattices *Science* **333** 996

[17] Struck J, Ölschläger C, Weinberg M, Hauke P, Simonet J, Eckardt A, Lewenstein M, Sengstock K and Windpassinger P 2012 Tunable gauge potential for neutral and spinless particles in driven optical lattices *Phys. Rev. Lett.* **108** 225304
[18] Oka T and Aoki H 2009 Photovoltaic Hall effect in graphene *Phys. Rev.* B **79** 081406(R)
[19] Goldman N, Dalibard J, Aidelsburger M and Cooper N R 2015 Periodically driven quantum matter: the case of resonant modulations *Phys. Rev.* A **91** 033632
[20] Parker C V, Ha L-C and Chin C 2013 Direct observation of effective ferromagnetic domains of cold atoms in a shaken optical lattice *Nat. Phys.* **9** 769
[21] Ha L-C, Clark L W, Parker C V, Anderson B M and Chin C 2015 Roton-Maxon excitation spectrum of Bose condensates in a shaken optical lattice *Phys. Rev. Lett.* **114** 055301
[22] Zheng W and Zhai H 2014 Floquet topological states in shaking optical lattices *Phys. Rev.* A **89** 061603
[23] Zhang S-L and Zhou Q 2014 Shaping topological properties of the band structures in a shaken optical lattice *Phys. Rev.* A **90** 051601
[24] Creutz M 1999 End states, ladder compounds, and domain-wall fermions *Phys. Rev. Lett.* **83** 2636
[25] Bermudez A, Patanè D, Amico L and Martin-Delgado M A 2009 Topology-induced anomalous defect production by crossing a quantum critical point *Phys. Rev. Lett.* **102** 135702
[26] Mazza L, Bermudez A, Goldman N, Rizzi M, Martin-Delgado M A and Lewenstein M 2012 An optical-lattice based quantum simulator for relativistic field theoreis and topological insulators *New J. Phys.* **14** 015007
[27] Li X, Zhao E and Liu W V 2012 Topological states in a ladder-like optical lattice containing ultracold atoms in higher orbital bands *Nat. Commun.* **4** 1523
[28] Sticlet D, Seabra L, Pollmann F and Cayssol J 2014 From fractionally charged solitons to Majorana bound states in a one-dimensional interacting model *Phys. Rev.* B **89** 115430
[29] Mazza L, Aidelsburger M, Tu H-H, Goldman N and Burrello M 2015 Methods for detecting charge fractionalization and winding numbers in an interacting fermionic ladder *New J. Phys.* **17** 105001
[30] Jünemann J, Piga A, Ran S-J, Lewenstein M, Rizzi M and Bermudez A 2017 Exploring interacting topological insulators with ultracold atoms: the synthetic Creutz-Hubbard model *Phys. Rev.* X **7** 031057
[31] Barbarino S, Rossini D, Rizzi M, Fazio R, Santoro G E and Dalmonte M 2019 Topological devil's staircase in atomic two-leg ladders *New J. Phys.* **21** 043048
[32] Hügel D and Paredes B 2014 Chiral ladders and the edges of quantum Hall insulators *Phys. Rev.* A **89** 023619
[33] Hughes T L, Prodan E and Bernevig B A 2011 Inversion-symmetric topological insulators *Phys. Rev.* B **83** 245132
[34] Li L and Chen S 2015 Hidden-symmetry-protected topological phases on a one-dimensional lattice *Eur. Phys. Lett.* **109** 40006
[35] Celi A, Massignan P, Ruseckas J, Goldman N, Spielman I B, Juzeliūnas G and Lewenstein M 2014 Synthetic gauge fields in synthetic dimensions *Phys. Rev. Lett.* **112** 043001
[36] Goldman N and Dalibard J 2014 Periodically driven quantum systems: effective Hamiltonian and engineered gauge fields *Phys. Rev.* X **4** 031027
[37] Eckardt A and Anisimovas E 2015 High-frequency approximation for periodically driven quantum systems from a Floquet-space perspective *New J. Phys.* **17** 093039
[38] Bukov M, D'Alessio L and Polkovnikov A 2015 universal high-frequency behavior of periodically driven systems: from dynamical stabilization to Floquet engineering *Adv. Phys.* **64** 139
[39] Lee M, Han J H, Kang J H, Kim M-S and Shin Y 2017 Double resonance of Raman transitions in a degenerate Fermi gas *Phys. Rev.* A **95** 043627
[40] Greiner M, Bloch I, Mandel O, Hänsch T W and Esslinger T 2001 Exploring phase coherence in a 2D lattice of Bose–Einstein condensates *Phys. Rev. Lett.* **87** 160405
[41] Reitter M, Näger J, Wintersperger K, Sträter C, Bloch I, Eckardt A and Schneider U 2017 Interaction dependent heating and atom loss in a periodically driven optical lattice *Phys. Rev. Lett.* **119** 200402
[42] Sun N and Lim L-K 2017 Quantum charge pumps with topological phases in a Creutz ladder *Phys. Rev.* B **96** 035139
[43] Neupert T, Santos L, Chamon C and Mudry C 2011 Fractional quantum Hall states at zero magnetic field *Phys. Rev. Lett.* **106** 236804
[44] Bergholtz E J and Liu Z 2013 Topological flat band models and fractional Chern insulators *Int. J. Mod. Phys.* B **27** 1330017
[45] Goldman N, Gerbier F and Lewenstein M 2013 Realizing non-Abelian gauge potentials in optical square lattices: an application to atomic Chern insulators *J. Phys. B: At. Mol. Opt. Phys.* **46** 134010
[46] Liu X-J, Liu X, Wu C and Sinova J 2010 Quantum anomalous Hall effect with cold atoms trapped in a square lattice *Phys. Rev.* A **81** 033622
[47] Zak J 1989 Berry's phase for energy bands in solids *Phys. Rev. Lett.* **62** 2747